Energy & Environmental Science

ROYAL SOCIETY OF CHEMISTRY

PAPER

View Article Online
View Journal | View Issue

Check for updates

Cite this: *Energy Environ. Sci.*, 2020, **13**, 1259

Visualizing morphological principles for efficient photocurrent generation in organic non-fullerene acceptor blends†

Wolfgang Köntges,[a] Pavlo Perkhun,[b] Jochen Kammerer,[c] Riva Alkarsifi,[b] Uli Würfel,[d] Olivier Margeat,[b] Christine Videlot-Ackermann,[b] Jean-Jacques Simon,[e] Rasmus R. Schröder,[cf] Jörg Ackermann*[b] and Martin Pfannmöller*[a]

Received 1st November 2019,
Accepted 20th February 2020

DOI: 10.1039/c9ee03535d

rsc.li/ees

The efficiency of organic solar cells with donor polymers and non-fullerene acceptors depends on a complex morphology. Similar chemical and electronic structures impede generating in-depth insights in morphological details. We visualise molecular arrangements and the nanomorphology in PBDB-T:ITIC blends by correlating transmission electron micrographs and material distribution maps. Material phases are identified by machine learning on hyperspectral data from electron spectroscopic imaging. We observe a specific polymorph of ITIC after thermal annealing. During annealing, enhanced by the presence of additives, PBDB-T acts as nucleation site for ITIC due to strong π–π-interactions of the electron withdrawing groups of both molecules. This leads to efficient charge transport paths in ITIC phases with direct π–π-contact to PBDB-T at the interface. We conclude that π–π-stacking between donor and acceptor molecules facilitates charge carrier generation within mixed interface regions.

Broader context

A crucial step for the advancement of organic solar cells was made by introducing novel, versatile non-fullerene molecules. These materials still provide specific advantages, such as solution processing, or strongly reduced toxicity in processing and use. However, the nanoscale structural landscape that determines performance and understanding of photophysics is still not fully known. Elucidating this relation by applying electron microscopy (EM)—one of the major tools offering the required resolution—is hampered by the similarity of donor and acceptor molecules regarding chemical composition and electronic structure. We demonstrate that analytical EM enables materials phase identification at the nanometer scale. Interpretation of morphological details is augmented by correlating phase distribution maps with high-resolution information about crystallinity. Using the system PBDB-T:ITIC we experimentally show that ITIC acceptor molecules adopt the periodic spacing of the PBDB-T repetition units. This happens already in mixed interface regions and is facilitated by polymorphism of ITIC. Here, we demonstrate that these visualized crystallites only form under thermal treatment in the presence of PBDB-T. We were able to correlate these structural features to improved performance. We envision an in-depth understanding of both the influence of processing parameters and the relation between molecular structure and photophysics.

Introduction

Complex morphologies play a significant role for performance enhancements in solution-processed organic solar cells (OSCs) with the objective of low-cost fabrication. The bulk heterojunction composed of acceptor molecules blended with donor polymers maximizes the interfacial area for charge separation. However, structural parameters of the so-called blend across multiple length scales depend on the thermodynamic conditions and kinetics during processing.[1] Two factors are typically discussed, which are polymorphic structures in donor and acceptor domains, and molecular arrangements around interfaces. For fullerene-based OSCs, acceptor polymorphism and

[a] *CAM, Centre for Advanced Materials, Heidelberg University, Heidelberg, Germany. E-mail: m.pfannmoeller@fastmail.net*
[b] *Aix Marseille Univ, CNRS, CINaM, Marseille, France. E-mail: jorg.ackermann@univ-amu.fr*
[c] *3DMM2O, Cluster of Excellence (EXC-2082/1 – 390761711) and CAM – Centre for Advanced Materials, Heidelberg University, Heidelberg, Germany*
[d] *Fraunhofer Institute for Solar Energy Systems ISE, Freiburg, Germany and Freiburg Materials Research Center FMF, University of Freiburg, Freiburg, Germany*
[e] *Aix Marseille Univ, Université de Toulon, CNRS, IM2NP, Marseille, France*
[f] *3DMM2O, Cluster of Excellence (EXC-2082/1 – 390761711) and Cryo Electron Microscopy, BioQuant, University Heidelberg, University Hospital, Heidelberg, Germany*

† Electronic supplementary information (ESI) available. See DOI: 10.1039/c9ee03535d

Open Access Article. Published on 21 February 2020. Downloaded on 1/12/2026 2:27:36 AM.
This article is licensed under a Creative Commons Attribution-NonCommercial 3.0 Unported Licence.

Open Access Article. Published on 21 February 2020. Downloaded on 1/12/2026 2:27:36 AM.
This article is licensed under a Creative Commons Attribution-NonCommercial 3.0 Unported Licence.

its manipulation is well studied.[2] In comparison to fullerenes with globular chemical structure and isotropic electron transport properties, small, more planar molecules are more susceptible to inefficient charge transport due to unfavourable molecular arrangements. The overlap of π-orbitals strongly depends on specific orientations.[3] In addition, the adaption of theories about electronic coupling between donor and acceptor groups[4] is crucial to understanding charge-carrier generation at interfaces.[5] Nevertheless, non-fullerene acceptors (NFAs) have enabled an increase in power conversion efficiencies (PCEs) to more than 16%[6] in single junction cells. NFAs based on molecular acceptor–donor–acceptor architectures, such as ITIC,[7] primarily contribute to the current breakthroughs. Underlying advantages of NFAs are the tunability of energy levels, complementary light absorption and planarity of molecules or sub-units.[8–10] The theoretical PCE limit for NFA-based single junction cells is estimated to be around 20%.[11] However, to approach this limit in PCE, it is essential to understand the most significant performance driving factors connected to the morphology.[12,13]

The NFA molecule ITIC receives special attention because of its relatively high charge-carrier mobility, and thermal and mechanical stability.[14,15] A widely studied donor:acceptor pair is PBDB-T:ITIC[15] and can thus serve as model system for morphological analyses. Fig. 1a and Fig. S1 (ESI†) show the chemical structures and Fig. 1b illustrates the most important charge transfer and transport processes within an NFA-based OSC. However, molecular arrangements at the interface and within the acceptor phase have been elusive because direct or experimental evidence is lacking. Clear distinction between donor and acceptor with existing microscope techniques is aggravated by the similar electronic structures. In this work, we determine the molecular arrangement of ITIC and PBDB-T in photovoltaic blends by analytical transmission electron microscopy (ATEM). Material distribution maps from nanoscale analytical imaging were correlated with bright-field information on ordered domains with a spatial resolution of up to 1.45 nm. We show that additive assisted processing leads to moderate increase in domain sizes. In addition, ITIC molecules adapt a single backbone-to-backbone spacing after thermal annealing similar to the length of the repeating unit of PBDB-T, which was predicted by molecular dynamics simulations.[16] We infer that an ITIC polymorph with chain-like conformation is present after thermal annealing, favouring docking to PBDB-T by arrangement of the electron withdrawing groups of both molecules at the interface.[17] This ITIC reorganization leads to higher short-circuit current densities. Our results suggest that optimal π-orbital overlapping is crucial for charge-carrier generation. This contrasts with most polymer:fullerene BHJs.[18,19]

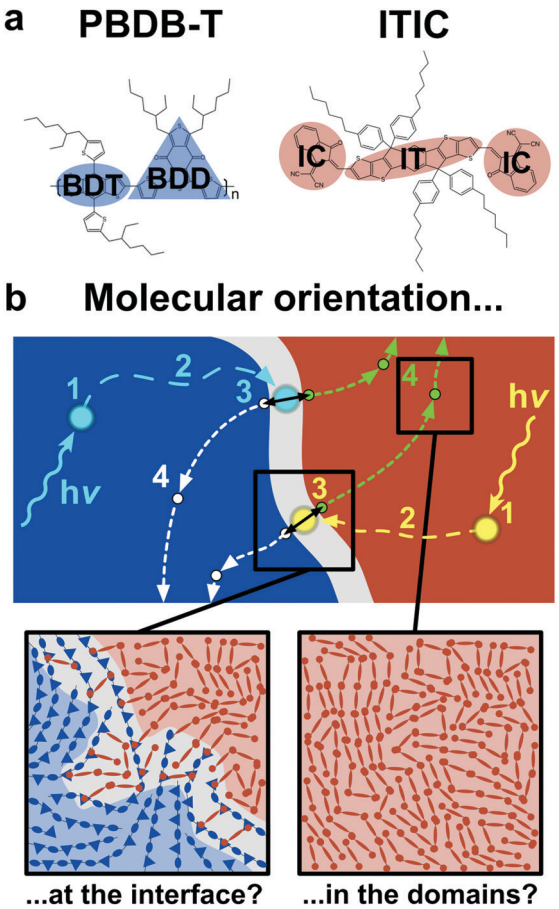

Fig. 1 Schematic illustration of a bulk hetero junction absorber layer of an organic solar cell. (a) Chemical structures of the polymer PBDB-T and the non-fullerene acceptor ITIC overlaid by a schematic representation indicating the IT backbone and the IC end groups of ITIC. Similarly, the BDT and BDD moieties are illustrated to discern the electron donating and withdrawing unit of PBDB-T, respectively. (b) Most important opto-electronic processes within different material phases (1: photon absorption and exciton formation, 2: exciton diffusion, 3: exciton dissociation and 4: charge transport). The donor phase is represented by the blue area corresponding to PBDB-T polymers absorbing high energy photons. Similarly, the acceptor phase is represented by the brown area corresponding to ITIC molecules absorbing low energy photons. Additionally, a mixed phase is represented by the grey coloured area.

Results and discussion

Molecular organization in pure ITIC thin films

Efficient charge transport is typically attributed to the existence of crystals within a photoactive film. For ITIC, it was shown through molecular dynamics simulations that the molecular packing within a thin film might be different from an ITIC crystal in bulk.[16] Therefore, we investigated pure ITIC films of *ca.* 30 nm thickness with intermediate-resolution TEM and electron diffraction (ED). Well oriented crystals are visible in bright-field TEM images due to phase contrast. Fig. 2 and Fig. S2 (ESI†) show that ITIC forms crystallites within the thin films. TEM images and corresponding power spectra of crystalline regions suggest a broad range of possible crystallographic spacings for ITIC from 1.4–2.2 nm (Fig. 2a–c). The lattice parameters of ITIC, as determined from single crystal X-ray diffraction,[16] are a = 1.49 nm, b = 1.55 nm and c = 1.81 nm. ED patterns in Fig. 2g and h show several sharp reflections at a lattice distance of 1.45 nm, which we assign to the (100) plane

This journal is © The Royal Society of Chemistry 2020

Open Access Article. Published on 21 February 2020. Downloaded on 1/12/2026 2:27:36 AM.
This article is licensed under a Creative Commons Attribution-NonCommercial 3.0 Unported Licence.

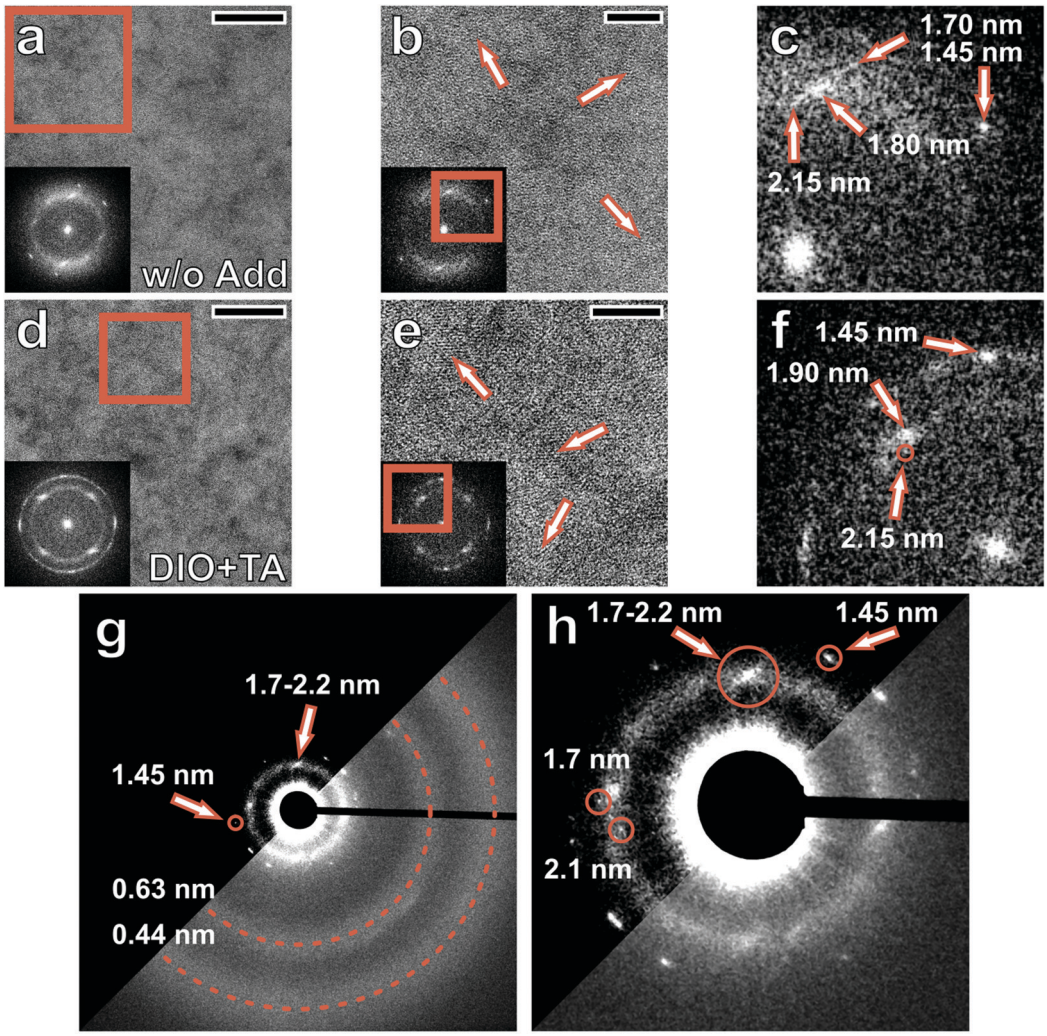

Fig. 2 Bright-field TEM images and electron diffraction (ED) patterns of 30 nm thin ITIC films show a large range of periodic spacings. (a) Bright-field TEM image of ITIC with the inserted power spectrum and a frame indicating the area enlarged in (b). (b) Enlarged area from (a) with its inserted power spectrum. The arrows mark regions of ordered packed ITIC molecules. (c) Magnified region of the power spectrum in (b) showing the spatial frequency range from 1.45–2.15 nm of different periodic structures in the image. (d–f) The corresponding images as in (a–c) for a 30 nm thin ITIC film processed with DIO in combination with thermal annealing. (g) ED pattern of the same ITIC sample as in (a) at another sample position with diffraction signals consistent with the results from (a–f). Additional rings at 0.63 nm and 0.44 nm arising from π–π-stacking are indicated. (h) Centre region of the ED pattern in (g) showing strong reflections (indicated by circles) arising from small crystallites of different lattice spacing within the range of 1.45 nm to 2.2 nm. Scalebars in (a and d) represent 100 nm, in (b and e) 30 nm.

of the triclinic single crystal structure. The absence of the (010) reflection can be explained by its weak structure factor (data not shown). The broad ring at 1.7–2.2 nm contains sharp reflections from the (001) plane of the single crystal structure but also indicates the existence of amorphous structures with varying distances. These distances correspond to the varying backbone-to-backbone spacings of ITIC molecules in thin films, as predicted from molecular dynamics.[16] The ED pattern in Fig. 2g further shows two broader rings below distances of 0.75 nm, which can be attributed to the π–π-stacking distance of the IC units. For an ITIC film fabricated with 0.5 vol% diiodooctane (DIO) as solvent additive and thermal annealing at 140 °C for 15 min the order is increased but similar lattice distances are observed (Fig. 2d–f). This indicates that these processing conditions do not significantly alter the molecular arrangement in a pure ITIC film.

Ordering and phase arrangements in a non-annealed blend

The analysis for ITIC discussed in Fig. 2 implies that the acceptor structures show spacings that are very similar to the lattice spacings of the donor polymer PBDB-T[20] (see Fig. S3, ESI†). Consequently, observation of phase contrast with spacings between 2.0–2.2 nm in bright-field images of a blend of both materials cannot be used to unambiguously identify the underlying material or phase. Therefore, we combined bright-field TEM with analytical TEM (ATEM) to obtain a comprehensive view of the morphological features. ATEM has been successfully applied to reveal the material phase

Open Access Article. Published on 21 February 2020. Downloaded on 1/12/2026 2:27:36 AM.
This article is licensed under a Creative Commons Attribution-NonCommercial 3.0 Unported Licence.

distribution of fullerene-based OSCs.[19,21–24] Nanoscale phase distribution maps of the photoactive layers can be obtained from machine learning algorithms for non-linear manifold learning.[19,25] We apply electron spectroscopic imaging (ESI) by recording inelastic images within the low-energy loss range using a stable imaging spectrometer. This allows detection of subtle, fingerprint-like differences in optical excitations of the different phases. Fundamentally, phases within a blend that show varying plasmon excitation signatures generate material contrast in specific inelastic images. So far it has not been obvious whether this imaging approach yields contrast at the required resolution between semiconducting polymers and small molecules. For instance, NFA acceptors are—unlike fullerenes[18,19]—close in electronic structure to their donor partner molecule. However, as shown in the normalized electron energy-loss spectra in Fig. S4 (ESI†), a shift of the $\sigma + \pi$ plasmon peak is observed between PBDB-T and ITIC even after initial damage by the primary electrons. An ESI data set in this energy range yields inverted contrasts and thus enables phase identification (Fig. S4 and Video S1, ESI†). Furthermore, the π plasmon signal of ITIC is much stronger than that for PBDB-T. This signal at around 6.5 eV disappears through beam damage but can be used in a first image of a series to unambiguously verify the contrast obtained from the irradiation-stable $\sigma + \pi$ plasmon signals between 10–30 eV.

To substantiate the outcomes of the imaging approach, we applied ESI imaging to a blend of PTB7-Th:ITIC-DM. The corresponding devices show low performance (Fig. S5, ESI†), which is addressed to a pronounced phase separation (Fig. S6, ESI†). This poor performance is in contrast to solar cells based on PBDB-T:ITIC-DM[26] and PTB7-Th:ITIC-Th blends (see Fig. S5, ESI†) suggesting that specifically the PTB7-Th:ITIC-DM blend shows low miscibility. In-depth analysis of the observed morphology and low performance values goes beyond the scope of this work. Nevertheless, the pronounced phase separation enables straightforward interpretation of ATEM results. For evidence of correct qualitative material phase assignments, we recorded elemental maps for sulphur and carbon from the excitation of their L-edge at 165 and K-edge at 285 eV, respectively, since the ratio of both elements varies between the donor and acceptor molecules. Typically, elemental mapping is not the preferred choice as source of material contrast due to its inferior signal to noise ratio compared to low-energy loss ESI.[27] However, for PTB7-Th:ITIC-DM in Fig. S6 and S7 (ESI†) the ratio of sulphur and carbon maps confirms the results obtained from low-energy loss features.

Fig. 3a shows a correlative overlay of a bright-field TEM image for a 30 nm thin PBTB-T:ITIC film and a map of segmented phases obtained from processing a low-energy loss ESI data set. The blend was not annealed but fabricated with DIO. As for fullerene-based blends,[19,22] functional phases are identified including a mixed phase (white in Fig. 3a–d) connecting pure domains (brown for ITIC and blue for PBDB-T). Fig. 3b–d shows three enlarged crystalline areas from Fig. 3a with different material phase assignments. From the corresponding power spectra in Fig. 3e–g the spacings of the periodic structures in the bright-field TEM image are determined. Ordered structures in donor and acceptor phases show spacings of 2.1 nm and 1.9 nm, respectively. Measurements of several crystalline areas (20 for ITIC and 6 for PBDB-T) consistently show similar values for the domains assigned to ITIC (Table S1, ESI†). In Fig. 3d, ignoring the material distribution map in the correlative overlay, one single crystallite would be assigned to this area. However, the power spectrum in Fig. 3g reveals the existence of two different periodic structures within the same area. An exact investigation of the subareas (Fig. S8, ESI†) implies that indeed Fig. 3d does not show a unique crystal but two adjacent PBDB-T and ITIC crystals.

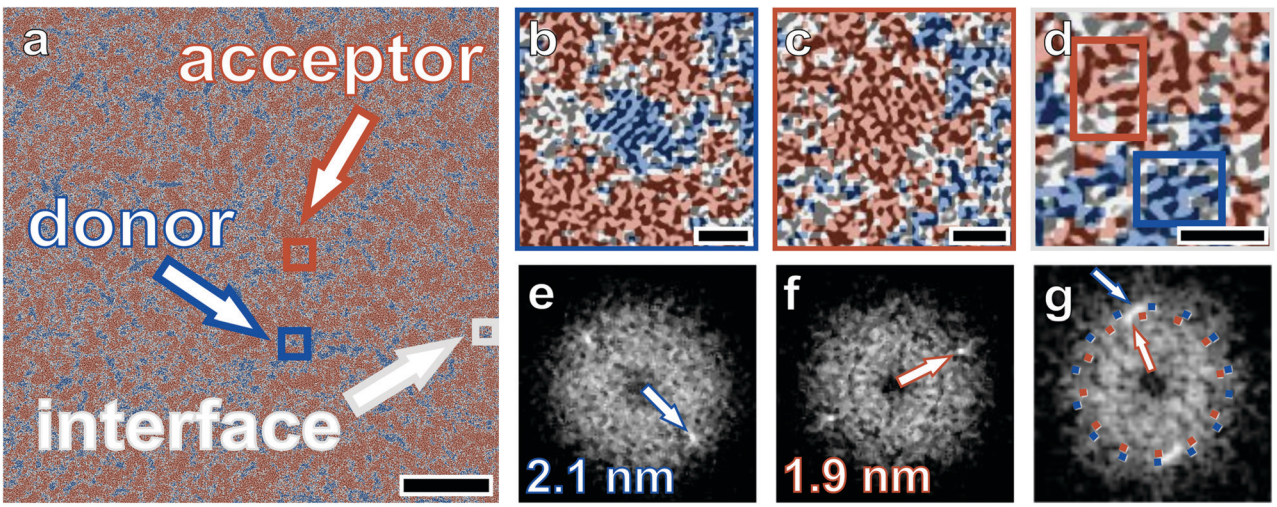

Fig. 3 Correlative analysis shows effects on crystallinity and materials phase distribution of ITIC when blended with PBDB-T using the additive DIO. (a) Correlative overlay of a bright-field TEM image and an analytical TEM (ATEM) material distribution map acquired from a 30 nm thin PBDB-T:ITIC layer with additive DIO processed without additional thermal annealing. (b–d) Images of crystalline areas assigned to donor (marked in blue) or acceptor (marked in brown) areas by ATEM. (e–g) Power spectra of the according areas in (b–d). Scalebars in (a) represents 200 nm, in (b–d) 10 nm.

 This journal is © The Royal Society of Chemistry 2020

Open Access Article. Published on 21 February 2020. Downloaded on 1/12/2026 2:27:36 AM.
This article is licensed under a Creative Commons Attribution-NonCommercial 3.0 Unported Licence.

In addition, the material phase assignment allows to exclude that variations in texture, *i.e.* crystal orientation, induce the differences in the observed lattice spacings in Fig. 3g.

Molecular dynamics simulations[16] indicated that ITIC molecules can take up several molecular arrangements, driven by strong π–π-interaction of the terminal IC groups. Backbone-to-backbone distances from 0.75–2.25 nm were predicted to be possible. The aggregates with short backbone-to-backbone distances are best described as cluster-like, whereas those with long backbone-to-backbone distances as chain-like. In ED, we observe a broad scattering background with various discrete reflections in the range of 1.7–2.2 nm in pure ITIC films and of 1.9–2.2 nm when blended with PBDB-T using DIO. We can infer that a chain-like orientation of ITIC molecules is preferred and several polymorphic crystal structures with varying backbone-to-backbone distance form within the thins films. In this sense, the centre of mass distances from backbone-to-backbone also induce variations of the π–π-stacking distances of the terminal IC groups.[16] The single crystal (100) reflection could neither be observed in the bright-field images nor in the diffraction patterns of any blend. This implies the complete absence of the single crystal structure of ITIC when blended in thin films.

Impact of additives and thermal annealing on molecular orientation

For an in-depth understanding of processing parameters on molecular orientation in different phases, we investigate effects of thermal annealing in combination with additives. One layer was processed without and two layers with either the additive DIO or chloronaphthalene (CN). Solar cell parameters of the three corresponding devices (averages of n = 6–10) are shown in Table 1 and current density–voltage curves for best cells in Fig. S9 (ESI†). Thermal annealing leads to an increase in both fill factor and short-circuit current whereas additive assisted processing induces higher fill factors. Thereby the effect of additives is enhanced by annealing. Since annealing and application of additives are steps designed to change the morphology, visualization is essential to establish structure–property relations. We note that for solar cell characterization active layer thicknesses of around 100 nm were used whereas TEM analyses were performed on 30 nm layers. The latter allows unambiguous assignment of materials phases as we thus minimize the volume, which is projected in a 2D image.[28] Although domain distributions and sizes may differ as a function of layer thickness, the focus of this work lies in the visualization of general structural features that can be expected to be identical in thicker layers. Each layer type was investigated by intermediate-resolution bright-field TEM, ED and ESI. Raw results are shown in Fig. S4 (ESI†). ED patterns for sizes smaller than or equal to 1 nm appear to be a superposition of the reference patterns. This is not the case for values larger than 1 nm. In this range only two rings in the ED patterns are visible, around 1 nm and 2.2 nm. Features at 1.0 nm are generated by PBDB-T. However, it is not possible to unequivocally assign features at 2.2 nm to either donor or acceptor. This distance roughly corresponds to the PBDB-T (100) spacing[20,29] as well as to possible backbone-to-backbone distances of ITIC[16,17] as shown in Fig. 2 and 3. In Fig. 4a, f and k we show material distribution maps obtained from ESI data sets for the cases of layers processed without additive, DIO or CN, respectively. The maps are overlaid with bright-field TEM images, which reveals material assignments to crystallites. Fig. 4b–e provides enlargements of selected crystallites with corresponding power spectra for the additive-free layer. Likewise, crystallites are selected for the layer with DIO (Fig. 4g–j) and CN (l–o). Irrespective of the material assignment, all periodic distances are determined to be between 2.1–2.2 nm. However, the correlative results from ATEM enable identification of the material generating a specific crystallite. The unique occurrence of a spacing of 2.1–2.2 nm after thermal annealing suggests that the molecular arrangements of ITIC entirely adapts to the repetition unit distance of PBDB-T. This leads to a restriction to chain-like orientations of acceptor molecules,[16] which would provide isotropic charge transport through π–π-stacking of the IC domains in amorphous domain regions. The impact of reorganization of ITIC through thermal annealing is reflected in an increase in short-circuit current. The fill factor is not affected (examples 1 and 3 in Table 1). In contrast, blends show an additional increase in fill factor when thermal annealing is combined with application of additives (examples 2, 4 and 5 in Table 1).

The overlays in Fig. 4 show distributions and sizes of PBDB-T, ITIC, and intermixed phases. In fullerene-based blends, additives can have a major impact on morphology and performance, in particular through interaction with fullerene molecules.[30–32] Here, in combination with thermal annealing additives induce moderate enlargements of pure material domains for the PBDB-T:ITIC blends (see Fig. 4). Characteristic domain sizes as determined from the material distribution maps increase from a range of 5–67 nm to 14–67 nm or 33–67 nm with DIO or CN, respectively (see Fig. S10, ESI†). Another impact of additive assisted processing on the NFA phase in the blends is the improvement of the degree of crystallinity in the ITIC phase (see Fig. 4 and Fig. S3, ESI†). Both additive induced processes might be related to increased

Table 1 Influence of thermal annealing and solvent additives on performance. Photoelectric parameters are provided for PBDB-T:ITIC based OSCs under optimized fabrication conditions under illumination

#: Blend (additive)	V_{oc} [V]	J_{sc} [mA cm^{-2}]	FF	PCE_{max} [%]	PCE_{avg} [%] (# cells)	Annealed
1: PBDB-T:ITIC (without)	0.89	12.80	0.50	5.68	5.61 ± 0.05 (3)	No
2: PBDB-T:ITIC (DIO)	0.89	13.44	0.53	6.44	6.34 ± 0.07 (6)	No
3: PBDB-T:ITIC (without)	0.85	15.30	0.50	7.19	6.57 ± 0.32 (6)	Yes
4: PBDB-T:ITIC (DIO)	0.86	15.00	0.65	8.65	8.57 ± 0.21 (10)	Yes
5: PBDB-T:ITIC (CN)	0.88	14.40	0.61	8.08	7.70 ± 0.30 (6)	Yes

Open Access Article. Published on 21 February 2020. Downloaded on 1/12/2026 2:27:36 AM.
This article is licensed under a Creative Commons Attribution-NonCommercial 3.0 Unported Licence.

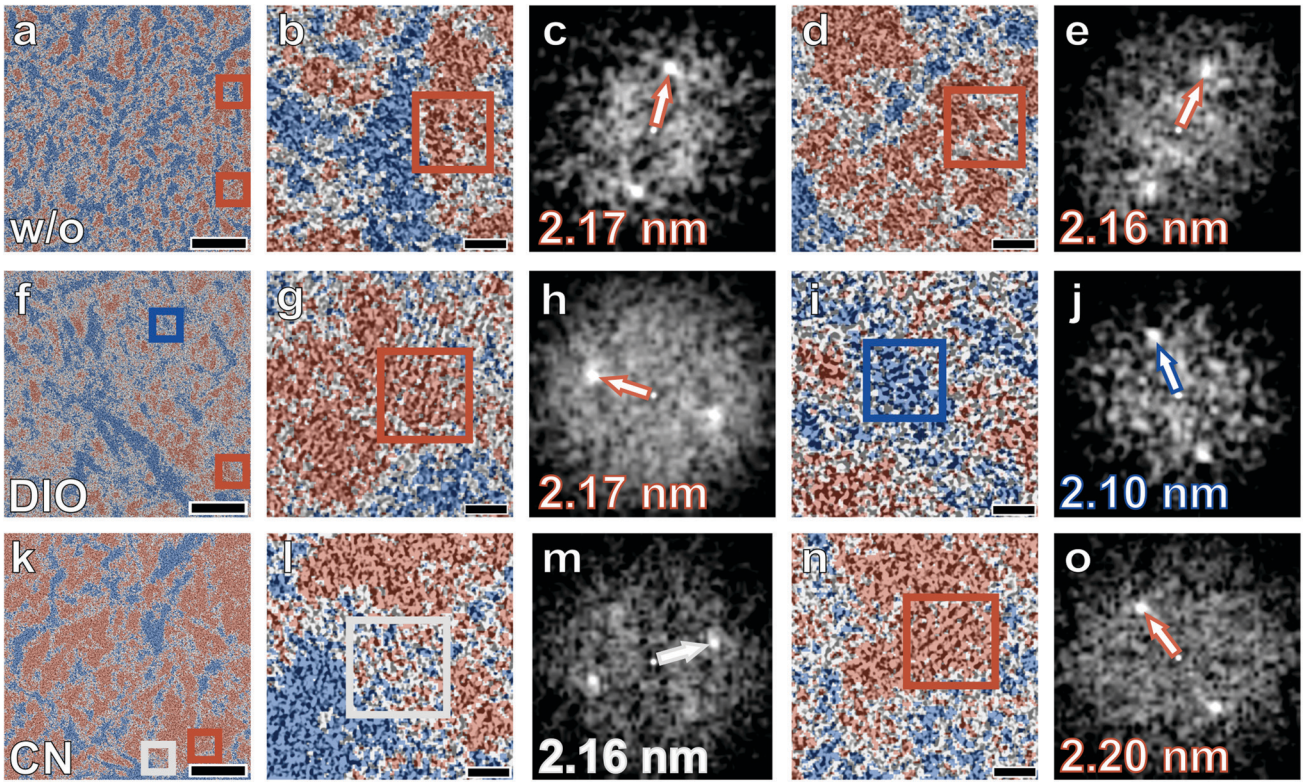

Fig. 4 Correlative analysis reveals molecular arrangements of ITIC at interfaces to PBDB-T and in acceptor domains after thermal annealing. (a–e) Blend fabricated without solvent additive. (b) and (d) show enlarged regions marked in (a). (c) and (e) show the calculated power spectra from the crystalline regions marked in (b) and (d), respectively. In both power spectra a periodic structure with a lattice spacing of more than 2.1 nm is indicated. (f–j) Corresponding images for a PBDB-T:ITIC blend processed with DIO showing a crystalline acceptor area and donor area in (g) and (i), respectively. (k–o) Corresponding images for a PBDB-T:ITIC blend processed with additive CN. Scalebars in (a, f and k) represent 100 nm and 10 nm in enlarged overlay images.

average domain purity, which was shown to occur in some NFA based blends upon additive use and is related to lower geminate and non-geminate recombination and hence to enhanced fill factors.[33] Although the amount of mixed phase calculated from the material distribution maps could provide indications to average purity, here resonant soft X-ray scattering would aid to obtain a complete view.[33] Nevertheless, the observed domain enlargement and increased ordering indicates improved charge-carrier transport with less accumulation of charge-carriers and hence less recombination for a given external voltage.[34]

Fig. 4 shows that intermixed materials at the interfaces between donor and acceptor domains are found to extent to a few nanometers. Furthermore, we observe for PBDB-T:ITIC blends that after thermal annealing the crystals with 2.1–2.2 nm spacing emanate from the (mixed) donor:acceptor interface into the ITIC phase (see Fig. 4l). This indicates that blends of polymers and ITIC derivatives behave differently from fullerene-based blends, in which amorphous mixed phases were repeatedly found to be larger and advantageous in providing energy cascades for charge-carrier generation.[22,35–37] Han and co-workers performed atomistic simulations of the PBDB-T:ITIC interface blend.[17] They predicted that the combination of using the additive DIO and thermal annealing favours a docking of the IC moieties to the electron withdrawing BDD unit of the polymer. Thus, thermal annealing under the use of DIO or CN induces the nucleation of ITIC crystals at PBDB-T. In this way chains of ITIC molecules in face-on orientation can start growing from the BDD unit of the polymer into the pure acceptor phase, which promotes exciton dissociation[17] through π–π-interactions. This suggests that charge-carrier generation in ITIC-based OSCs is facilitated by dissociation through hot state charge delocalization[38] in conjunction with energy cascade effects from mixed towards pure phases. The impact of additives and thermal annealing on molecular arrangement that were deciphered for PBDB-T:ITIC are schematically summarized in Fig. 5. The crystalline domain corresponds to the here observed polymorph of ITIC, which is unique to thin films and the presence of PBDB-T as nucleation site and promoted by thermal annealing and the process additives.

Direct visualization of donor acceptor domains in annealed blends has been achieved together with unequivocal assignment of crystallites with lattice spacings of around 2.15 nm to ITIC. Since PBDB-T forms crystals with similar lattice spacing, an assignment of the materials based on the observed crystallites is ambiguous. Bulk measurements such as X-ray diffraction are essential in deciphering structural properties[29,33] but the assignment of crystalline features to the correct material is not straightforward. With respect to the diffraction results alone in Fig. 2,

 This journal is © The Royal Society of Chemistry 2020

Open Access Article. Published on 21 February 2020. Downloaded on 1/12/2026 2:27:36 AM.
This article is licensed under a Creative Commons Attribution-NonCommercial 3.0 Unported Licence.

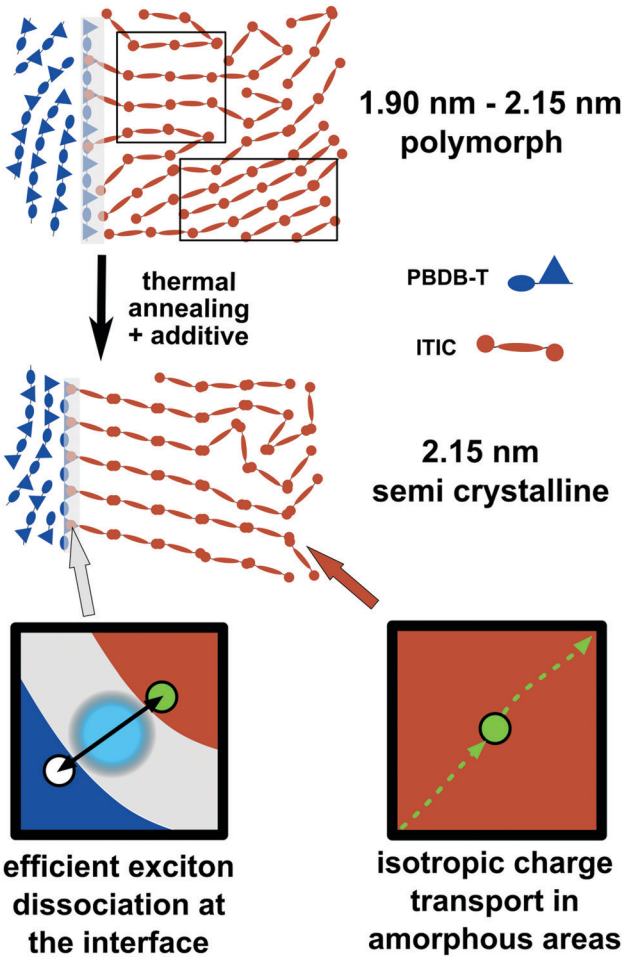

Fig. 5 Schematic illustration of the optimal morphology of an organic solar cell based on the system PBDB-T:ITIC. The rearrangement of the ITIC molecules from a polymorphic (lattice spacings from 1.90 nm to 2.15 nm) to a semi crystalline structure (lattice spacing of around 2.15 nm) adapting the PBDB-T structural spacing through thermal annealing yields a morphology for efficient exciton dissociation and isotropic charge transport. The schematic representation of both PBDB-T polymer and ITIC molecules is adapted from Fig. 1.

X-ray measurements[29] by Liang *et al.* appear to confirm the results of Fig. 3. Here, we observe a similar crystallinity of PBDB-T:ITIC blends, which would be expected from the combined reference measurements of the pure materials. However, interpretations from the non-annealed layer in Fig. 3 as well as the X-ray diffraction[29] would lead to contradictory conclusions about the narrow range of spacings found in Fig. 4 after thermal annealing.

Adding the capabilities of spatially resolved ATEM in the low-energy-loss range and machine learning methods enables unequivocal assignments of material phases to crystalline and amorphous structures. Thereby, we expect that these material assignments are not significantly influenced by overlapping signals in two-dimensional TEM and ATEM projections from the three-dimensional material distribution. Although noise and outliers for single pixels cannot be excluded, as shown for P3HT:PCBM, the algorithm evaluating spectral differences primarily detects interface regions encircling pure and enriched domains.[39]

Conclusions

In most fullerene-based cells, efficient charge separation of excitons at the donor:acceptor interface requires substantial driving forces, *i.e.* an energetic difference between the LUMO levels of donor and acceptor, which lower the achievable open-circuit voltages. Reducing the driving forces by optimizing energy level alignment increases the attainable voltage but typically leads to strong losses in fill factor and short-circuit current density because of elevated geminate recombination. In the case of non-fullerene acceptors, there are several studies reporting high photocurrent densities despite low driving forces.[40–42] Optimal molecular arrangements might primarily contribute to this behaviour. Non-fullerene acceptors are versatile but challenging molecules with regards to the morphological parameter space.[12] However, we have shown by correlative imaging at the nanoscale that this versatility is one of their significant advantages. In PBDB-T:ITIC, previously unexpected polymorphic and interfacial structures lead to enhanced performance related to efficient charge-carrier generation and extraction. Owing to the relatively large LUMO level offset of 0.86 eV and the existence of mixed interface regions of several nanometers, we expect that charge-carrier generation is still supported by energy cascade processes. A crucial step towards understanding the different ways of efficient charge separation in relation to the morphology will be the in-depth and nanoscale visualisation of the low driving force systems.

To reach 20% efficiency and beyond, it is essential to find novel matching donor:acceptor pairs, in terms of energy level alignment but also in terms of miscibility[1] and potential for optimal molecular alignment. Solving the latter has been a demand in most recent works on NFAs to support rational design of the involved materials. Furthermore, research is aiming for a fabrication of OSCs by straightforward large-scale processing steps. This includes avoiding solvent additives. It was shown for PBDB-T:ITIC that efficiencies of $>10\%$ can be obtained by thermal and solvent vapour annealing.[29] Moreover, more recent material systems such as PM6:Y6 have demonstrated high efficiency of more than 15% without additives.[43] Correlative, high-resolution imaging analyses of such systems will provide valuable insights into morphological factors in combination to the results presented in the work at hand. Notably, material distribution maps can be applied to extract quantitative measures describing domain sizes, domain connectivity or domain shapes. However, correlative TEM/ATEM imaging will reveal more detailed insights into the relation of solution fabrication processes and post-treatment procedures such as domain interface or ordering characteristics.

Methods

Fabrication of the solar cells

First, ITO substrates (purchased from LUMTEC, 15 Ohm sq^{-1}) were thoroughly cleaned by sonication in acetone and ethanol

Open Access Article. Published on 21 February 2020. Downloaded on 1/12/2026 2:27:36 AM.
This article is licensed under a Creative Commons Attribution-NonCommercial 3.0 Unported Licence.

followed by rinsing with water and sonication in isopropanol and applying ultraviolet-ozone for 10 min. A thin layer of poly-(3,4-ethylenedioxythiophene) polystyrene sulfonate (PEDOT:PSS) (CLEVIOS™ AI 4083) was spin-coated on the cleaned ITO precoated glass substrate inside of argon-filled glove box at a speed of 3500 rpm for 60 s followed by heating on a hot-plate at 140 °C for 15 min. Three different blend solutions of PBDB-T:ITIC (materials purchased from 1-Material) for the photoactive layer were used: (i) 10 : 10 mg ml^{-1} in chlorobenzene without additives, (ii) 10 : 10 mg ml^{-1} in 99% vol chlorobenzene and 1% vol 1,8-diiodooctane (DIO) (iii) 10 : 10 mg ml^{-1} in 97% vol chlorobenzene and 3% vol 1-chloronaphthalene (CN). The PTB7-Th:ITIC-DM (1-Material) blend solution was prepared with 10 : 10 mg ml^{-1} ratio in chlorobenzene with 1% DIO. The PBDB-T:ITIC and PTB7-Th:ITIC-DM active blend layers, with a nominal thickness of 100 nm, were prepared by spin-coating at 2200 rpm for 2 min. After that, some layers were thermally annealed at 140 °C for 15 min and the other part was used as-cast without annealing. A more detailed description of the used materials PBDB-T, PTB7-Th, ITIC and ITIC-DM can be found in Fig. S1 (ESI†). After active layer deposition, ZnO nanoparticles in isopropanol and 0.2% (v/v) ethanol amine were spin-coated on the top of active layers at 3000 rpm for 1 min and dried on a hot plate at 140 °C for 5 min. All processes were performed inside a glove box. For processing the cathode, Al metal electrodes (100 nm) were thermally evaporated at 1×10^{-7} mbar through a shadow mask to obtain a device area of 0.27 cm^2.

Characterization

The current density–voltage (*J–V*) characteristics of the devices were measured using a Keithley 238 Source Measure Unit inside the glove box. Solar cell performance was measured using a Newport class AAA 1.5 Global solar simulator (Oriel Sol3ATM-model no 94043A) with an irradiation intensity of 100 mW cm^{-2}. The light intensity was determined with a Si reference cell (Newport Company, Oriel no 94043A) calibrated by the National Renewable Energy Laboratory (NREL).

Fabrication of the layers for ATEM

The ITO substrates were cleaned and covered with PEDOT in an identical way described in the section of the fabrication of the solar cells. Thin layers of the different blend and pure material solutions with a nominal thickness of 30 nm were prepared by spin-coating at 9500 rpm for 2 min and—where indicated—thermally annealed at 140 °C for 15 min. When fabricating layers with additives, ITIC solutions were prepared with 1% vol DIO or CN before spin-coating.

Sample preparation and morphological analysis

The photoactive layers and pure material layers (PBDB-T, PTB7-Th, ITIC and ITIC-DM) were floated upon demineralized water by dissolving the PEDOT:PSS layer and collected with holey carbon grids (QUANTIFOIL®). TEM measurements (bright-field TEM, ESI, EELS) were performed with a Cs aberration corrected Libra 200 MC (Carl Zeiss Microscopy GmbH, Germany) at 200 kV equipped with an in-column energy filter and a monochromator providing an energy resolution of better than 150 meV. Images were recorded at about Scherzer defocus with spherical aberration corrected to about 10 μm. EEL spectra were recorded from pure layers PBDB-T, PTB7-Th, ITIC and ITIC-DM with a thickness of around 30 nm and an energy resolution of 120 meV. The EEL spectra were normalized by the integral from 5 to 40 eV using HyperSpy.[44] For first EELS acquisition a total electron dose of 1500 electrons per nm^2 was applied. After a total dose of 150 000 electrons per nm^2 the signals below 10 eV changed through irradiation damage whereas the plasmon signals >10 eV show only minor shifts for much higher doses. Details on resulting spectra can be found in Fig. S4 (ESI†). ESI stacks were acquired from one layer of PTB7-Th:ITIC-DM and four layers of PBDB-T:ITIC. For ESI acquisition, image series were recorded from 5–40 eV in steps of 1 eV and a defocus between 0 to maximal −50 nm. As shown in eqn (S1) (ESI†), the signal delocalisation at spatial frequencies interpreted in this work – due to defocus, spherical aberration, and electron wavelength – is negligible (would amount to about −0.06 nm). Hence, locations of diffraction fringes in bright-field TEM images can be directly correlated with the material phase information. The slit aperture for inelastic images was set to a width of 1 eV. The total dose for each series was approximately 10×10^6 electrons per nm^2. The first image of a series was recorded at 0 eV to acquire a bright-field image for correlative analysis of crystallites. Preceding to data analysis, this bright-field image and inelastic images from the ESI series were aligned by affine image registration. The ESI series were normalized by the sum of all inelastic images in the series, *i.e.* the resulting integral equals 1, to remove the thickness and density contrast in the images and to reveal material contrasts. For noise reduction of the normalized ESI series principal component analysis was applied using Hyperspy.[44] Using *ilastik*, an open source software for image classification and segmentation based on statistical analysis and supervised machine learning,[45] the ESI spectra were classified into distinct classes. In the first step the dimensionality of the data is reduced by the application of locally linear embedding (LLE). In the second step, a random forest classifier is trained on the same label subsets to subsequently classify all remaining pixels or spectra yielding maps showing PBDB-T and ITIC domains as well as mixed or interface phases. The same procedure was applied to the PTB-7-Th:ITIC-DM dataset. Further details about this method are described elsewhere.[19] The elemental maps of the PTB-7-Th:ITIC-DM blends from sulphur and carbon ionization signals were generated using the three window method.[27] We note that although we used LLE within a custom software, several implementations exist for free-of-charge use, *e.g.*, for Matlab (MathWorks, USA) or for Python with the scikit-learn package. Thickness measurements were performed by the Fourier-log-ratio-method in the TEM[27] and structure-factors were assessed by JEMS-SAAS, a commercially available simulation software for electron microscopy by Pierre Stadelmann.

Author contributions

W. K., J. A. and M. P. designed the experiments. W. K. performed the experiments and data analysis. P. P. and R. A. fabricated the

 This journal is © The Royal Society of Chemistry 2020

Open Access Article. Published on 21 February 2020. Downloaded on 1/12/2026 2:27:36 AM.
This article is licensed under a Creative Commons Attribution-NonCommercial 3.0 Unported Licence.

organic layers for solar cells and TEM experiments and performed the solar cell fabrication and characterization under the supervision of O. M., C. V.-A., J.-J. S. and J. A. J. K. performed assessment of ITIC structure factors. J. K., U. W., C. V.-A., J.-J. S., O. M. and R. R. S. contributed to the interpretation of the data. W. K., M. P., J. A., P. P., J. K. and R. R. S. wrote the manuscript. All the authors discussed the results and contributed to revisions on the manuscript. The work was supervised by M. P., J. A. and R. R. S.

Conflicts of interest

There are no conflicts to declare.

Acknowledgements

This project has received funding by the Ministry of Science, Research and the Arts Baden-Württemberg, through the HEiKA materials research centre FunTECH-3D (MWK, 33-753-30-20/3/3) and from the European Union's Horizon 2020 research and innovation programme under the Marie Skłodowska-Curie grant agreement No. 713750. It has been carried out with the financial support of the Regional Council of Provence-Alpes-Côte d'Azur and with the financial support of the A*MIDEX (no. ANR-11-IDEX-0001-02), funded by the Investissements d'Avenir project funded by the French Government, managed by the French National Research Agency (ANR). This project has also received funding by the French Research Agency (projet ANR NFA-15). JK and RRS have been funded by the Deutsche Forschungsgemeinschaft (DFG, German Research Foundation) under Germany's Excellence Strategy *via* the Excellence Cluster 3D Matter Made to Order (EXC-2082/1 – 390761711). The authors acknowledge the data storage service SDS@hd supported by the Ministry of Science, Research and the Arts Baden-Württemberg and the German Research Foundation (DFG) through grant INST 35/1314-1 FUGG. The authors are grateful to Guangchao Han[16] for providing the CIF-file for ITIC single crystal characterization and Stefan Kauschke for the support on enabling sample preparation.

Notes and references

1 L. Ye, W. Zhao, S. Li, S. Mukherjee, J. H. Carpenter, O. Awartani, X. Jiao, J. Hou and H. Ade, *Adv. Energy Mater.*, 2017, **7**, 1602000.
2 S. Izawa, K. Nakano, K. Suzuki, Y. Chen, T. Kikitsu, D. Hashizume, T. Koganezawa, T.-Q. Nguyen and K. Tajima, *Sci. Rep.*, 2018, **8**, 1–11.
3 Y. Diao, K. M. Lenn, W.-Y. Lee, M. A. Blood-Forsythe, J. Xu, Y. Mao, Y. Kim, J. A. Reinspach, S. Park, A. Aspuru-Guzik, G. Xue, P. Clancy, Z. Bao and S. C. B. Mannsfeld, *J. Am. Chem. Soc.*, 2014, **136**, 17046–17057.
4 X. Yi, B. Gautam, I. Constantinou, Y. Cheng, Z. Peng, E. Klump, X. Ba, C. H. Y. Ho, C. Dong, S. R. Marder, J. R. Reynolds, S.-W. Tsang, H. Ade and F. So, *Adv. Funct. Mater.*, 2018, **28**, 1802702.
5 A. Devižis, J. De Jonghe-Risse, R. Hany, F. Nüesch, S. Jenatsch, V. Gulbinas and J.-E. Moser, *J. Am. Chem. Soc.*, 2015, **137**, 8192–8198.
6 B. Fan, D. Zhang, M. Li, W. Zhong, Z. Zeng, L. Ying, F. Huang and Y. Cao, *Sci. China: Chem.*, 2019, **62**, 746–752.
7 Y. Lin, J. Wang, Z.-G. Zhang, H. Bai, Y. Li, D. Zhu and X. Zhan, *Adv. Mater.*, 2015, **27**, 1170–1174.
8 P. Cheng, G. Li, X. Zhan and Y. Yang, *Nat. Photonics*, 2018, **12**, 131–142.
9 C. B. Nielsen, S. Holliday, H.-Y. Chen, S. J. Cryer and I. McCulloch, *Acc. Chem. Res.*, 2015, **48**, 2803–2812.
10 C. Yan, S. Barlow, Z. Wang, H. Yan, A. K.-Y. Jen, S. R. Marder and X. Zhan, *Nat. Rev. Mater.*, 2018, **3**, 18003.
11 J. Zhang, H. S. Tan, X. Guo, A. Facchetti and H. Yan, *Nat. Energy*, 2018, **3**, 720–731.
12 J. Hou, O. Inganäs, R. H. Friend and F. Gao, *Nat. Mater.*, 2018, **17**, 119–128.
13 S. M. Menke, N. A. Ran, G. C. Bazan and R. H. Friend, *Joule*, 2018, **2**, 25–35.
14 P. Sonar, J. P. F. Lim and K. Leok Chan, *Energy Environ. Sci.*, 2011, **4**, 1558–1574.
15 W. Zhao, D. Qian, S. Zhang, S. Li, O. Inganäs, F. Gao and J. Hou, *Adv. Mater.*, 2016, **28**, 4734–4739.
16 G. Han, Y. Guo, X. Song, Y. Wang and Y. Yi, *J. Mater. Chem. C*, 2017, **5**, 4852–4857.
17 G. Han, Y. Guo, X. Ma and Y. Yi, *Solar RRL*, 2018, **2**, 1800190.
18 S. Ben Dkhil, M. Pfannmöller, R. R. Schröder, R. Alkarsifi, M. Gaceur, W. Köntges, H. Heidari, S. Bals, O. Margeat, J. Ackermann and C. Videlot-Ackermann, *ACS Appl. Mater. Interfaces*, 2018, **10**, 3874–3884.
19 M. Pfannmöller, H. Flügge, G. Benner, I. Wacker, C. Sommer, M. Hanselmann, S. Schmale, H. Schmidt, F. A. Hamprecht, T. Rabe, W. Kowalsky and R. R. Schröder, *Nano Lett.*, 2011, **11**, 3099–3107.
20 W. Gao, T. Liu, R. Ming, Z. Luo, K. Wu, L. Zhang, J. Xin, D. Xie, G. Zhang, W. Ma, H. Yan and C. Yang, *Adv. Funct. Mater.*, 2018, **28**, 1803128.
21 D. M. DeLongchamp, R. J. Kline and A. Herzing, *Energy Environ. Sci.*, 2012, **5**, 5980–5993.
22 S. B. Dkhil, M. Pfannmöller, M. I. Saba, M. Gaceur, H. Heidari, C. Videlot-Ackermann, O. Margeat, A. Guerrero, J. Bisquert, G. Garcia-Belmonte, A. Mattoni, S. Bals and J. Ackermann, *Adv. Energy Mater.*, 2017, **7**, 1601486.
23 M. R. Hammond, R. J. Kline, A. A. Herzing, L. J. Richter, D. S. Germack, H.-W. Ro, C. L. Soles, D. A. Fischer, T. Xu, L. Yu, M. F. Toney and D. M. DeLongchamp, *ACS Nano*, 2011, **5**, 8248–8257.
24 W. Schindler, M. Wollgarten and K. Fostiropoulos, *Org. Electron.*, 2012, **13**, 1100–1104.
25 S. T. Roweis and L. K. Saul, *Science*, 2000, **290**, 2323–2326.
26 X. Du, T. Heumueller, W. Gruber, A. Classen, T. Unruh, N. Li and C. J. Brabec, *Joule*, 2019, **3**, 215–226.
27 R. F. Egerton, *Electron Energy-Loss Spectroscopy in the Electron Microscope*, Springer, New York, 3rd edn, 2011.
28 R. C. Masters, A. J. Pearson, T. S. Glen, F.-C. Sasam, L. Li, M. Dapor, A. M. Donald, D. G. Lidzey and C. Rodenburg, *Nat. Commun.*, 2015, **6**, 6928.

Open Access Article. Published on 21 February 2020. Downloaded on 1/12/2026 2:27:36 AM.
This article is licensed under a Creative Commons Attribution-NonCommercial 3.0 Unported Licence.

29 Q. Liang, J. Han, C. Song, X. Yu, D.-M. Smilgies, K. Zhao, J. Liu and Y. Han, *J. Mater. Chem. A*, 2018, **6**, 15610–15620.
30 E. Buchaca-Domingo, A. J. Ferguson, F. C. Jamieson, T. McCarthy-Ward, S. Shoaee, J. R. Tumbleston, O. G. Reid, L. Yu, M.-B. Madec, M. Pfannmöller, F. Hermerschmidt, R. R. Schröder, S. E. Watkins, N. Kopidakis, G. Portale, A. Amassian, M. Heeney, H. Ade, G. Rumbles, J. R. Durrant and N. Stingelin, *Mater. Horiz.*, 2014, **1**, 270–279.
31 S. Guo, E. M. Herzig, A. Naumann, G. Tainter, J. Perlich and P. Müller-Buschbaum, *J. Mater. Chem. B*, 2014, **118**, 344–350.
32 J. Kniepert, I. Lange, J. Heidbrink, J. Kurpiers, T. J. K. Brenner, L. J. A. Koster and D. Neher, *J. Mater. Chem. C*, 2015, **119**, 8310–8320.
33 X. Jiao, L. Ye and H. Ade, *Adv. Energy Mater.*, 2017, **7**, 1700084.
34 U. Würfel, D. Neher, A. Spies and S. Albrecht, *Nat. Commun.*, 2015, **6**, 1–9.
35 T. M. Burke and M. D. McGehee, *Adv. Mater.*, 2014, **26**, 1923–1928.
36 F. C. Jamieson, E. B. Domingo, T. McCarthy-Ward, M. Heeney, N. Stingelin and J. R. Durrant, *Chem. Sci.*, 2012, **3**, 485–492.
37 P. Westacott, J. R. Tumbleston, S. Shoaee, S. Fearn, J. H. Bannock, J. B. Gilchrist, S. Heutz, J. deMello, M. Heeney, H. Ade, J. Durrant, D. S. McPhail and N. Stingelin, *Energy Environ. Sci.*, 2013, **6**, 2756–2764.
38 A. A. Bakulin, A. Rao, V. G. Pavelyev, P. H. M. V. Loosdrecht, M. S. Pshenichnikov, D. Niedzialek, J. Cornil, D. Beljonne and R. H. Friend, *Science*, 2012, **335**, 1340–1344.
39 M. Pfannmöller, W. Kowalsky and R. R. Schröder, *Energy Environ. Sci.*, 2013, **6**, 2871–2891.
40 D. Baran, R. S. Ashraf, D. A. Hanifi, M. Abdelsamie, N. Gasparini, J. A. Röhr, S. Holliday, A. Wadsworth, S. Lockett, M. Neophytou, C. J. M. Emmott, J. Nelson, C. J. Brabec, A. Amassian, A. Salleo, T. Kirchartz, J. R. Durrant and I. McCulloch, *Nat. Mater.*, 2017, **16**, 363–369.
41 J. Liu, S. Chen, D. Qian, B. Gautam, G. Yang, J. Zhao, J. Bergqvist, F. Zhang, W. Ma, H. Ade, O. Inganäs, K. Gundogdu, F. Gao and H. Yan, *Nat. Energy*, 2016, **1**, 16089.
42 V. C. Nikolis, J. Benduhn, F. Holzmueller, F. Piersimoni, M. Lau, O. Zeika, D. Neher, C. Koerner, D. Spoltore and K. Vandewal, *Adv. Energy Mater.*, 2017, **7**, 1700855.
43 Q. An, X. Ma, J. Gao and F. Zhang, *Sci. Bull.*, 2019, **64**, 504–506.
44 F. D. L. Peña, E. Prestat, V. T. Fauske, P. Burdet, P. Jokubauskas, M. Nord, T. Ostasevicius, K. E. MacArthur, M. Sarahan, D. N. Johnstone, J. Taillon, J. Lähnemann, V. Migunov, A. Eljarrat, J. Caron, T. Aarholt, S. Mazzucco, M. Walls, T. Slater, F. Winkler, Pquinn-Dls, B. Martineau, G. Donval, R. McLeod, E. R. Hoglund, I. Alxneit, D. Lundeby, T. Henninen, L. F. Zagonel and A. Garmannslund, hyperspy/hyperspy: HyperSpy v1.5.2, Zenodo, 2019, DOI: 10.5281/zenodo.3396791.
45 C. Sommer, C. Straehle, U. Kothe and F. A. Hamprecht, Biomedical Imaging: From Nano to Macro, 2011 IEEE International Symposium on, 2011, 230–233, DOI: 10.1109/ISBI.2011.5872394.

This journal is © The Royal Society of Chemistry 2020